Conversion of Love waves in a forest of trees

Agnès Maurel
Institut Langevin, ESPCI ParisTech, CNRS, 1 rue Jussieu, 75005 Paris, France

Jean-Jacques Marigo
Laboratoire de Mécanique des Solides, Ecole Polytechnique, Route de Saclay, 91120 Palaiseau, France

Kim Pham
IMSIA, ENSTA ParisTech - CNRS - EDF - CEA, Université Paris-Saclay, 828 Boulevard des Maréchaux, 91732 Palaiseau, France

Sébastien Guenneau
Aix Marseille Univ., CNRS, Centrale Marseille, Institut Fresnel, 13013 Marseille, France

(Received 22 December 2017; revised manuscript received 11 October 2018; published 26 October 2018)

We inspect the propagation of shear polarized surface waves akin to Love waves through a forest of trees of the same height atop a guiding layer on a soil substrate. An asymptotic analysis shows that the forest behaves like an infinitely anisotropic wedge with effective boundary conditions. We discover that the foliage of trees brings a radical change in the nature of the dispersion relation of these surface waves, which behave like spoof plasmons in the limit of a vanishing guiding layer, and like Love waves in the limit of trees with a vanishing height. When we consider a forest with trees of increasing or decreasing height, this hybrid "spoof Love wave" is either trapped within the trees or converted into a downward propagating bulk (shear) wave. These mechanisms of wave trapping and wave conversion appear to be robust with respect to perturbations of height or position of trees in the metawedge and with respect to three-dimensional effects such as regarding a potential change of elastic wave polarization.

DOI: 10.1103/PhysRevB.98.134311

I. INTRODUCTION

Research in engineered metasurfaces has greatly benefited from the concept of surface waves supported by corrugated surfaces with Neumann boundary condition [1], called spoof plasmon polaritons in electromagnetism [2]. This has opened new vistas in the microwave regime and inspired further studies in plasmonics [3] and flat optics [4].

A particularly appealing object in this area is the so-called rainbow. In their seminal work [5], Tsakmakidis and coworkers demonstrated that the optical properties of surface electromagnetic waves can be tailored, by varying the surface nanotopology, via surface dispersion engineering. The resulting graded metasurface allows for light localization and segregation of different light colors [6], a concept which has found a counterpart for sound [7].

In the context of elasticity, previous studies focused on the case of polarized surface waves known as Rayleigh waves. Despite the differences between these mechanical waves and the electromagnetic waves, it has been shown that Rayleigh waves propagating over elastic crystals share common features with their electromagnetic counterparts, such as the existence of elastic Bragg band gaps [8]. These band gaps have been exploited to create a shielding effect for Rayleigh waves propagating at 50 Hertz through a soil structured with an array of boreholes [9]. Thanks to anomalous refraction [10], a lensing effect has been further observed for Rayleigh wave frequencies below 10 Hertz for an array of larger boreholes [11]. Recently, elastic resonant metasurfaces with subwavelength structurations have been considered and the concept of rainbow for optical waves has been translated to Rayleigh waves with the exciting application to the control of seismic surface waves [12–16]. The concept of seismic rainbow was first demonstrated for ultrasounds in experiments at the laboratory scale [15] and then extended up to the geophysical scale [12,16]. A forest densely populated with trees represents a naturally occurring geophysical metasurface for Rayleigh waves and an experiment in an actual forest environment [12,16] confirmed filtering properties due to the presence of stop bands around 100 Hertz. The dispersion relation derived in [14] revealed the existence of an effective wave that transitions from Rayleigh wavelike to shear wavelike behavior. The same effect was achieved with a metasurface consisting of subwavelength resonant elements buried under the soil surface [17]. These works opened the door to the development of seismic metasurfaces with the first realization of the so-called metawedge [15] and metabarrier [17] that are capable of mode converting the destructive surface seismic Rayleigh waves into mainly harmless downward-propagating bulk shear waves.

In this study, we show that such seismic metasurfaces can be designed for Love waves [18]. Love waves are shear polarized surface seismic waves, which produce a horizontal shaking that is particularly deleterious for the foundations of infrastructures [19–21]. Unlike for Rayleigh waves, Love waves require a guiding layer to propagate at the air-soil

 ©2018 American Physical Society

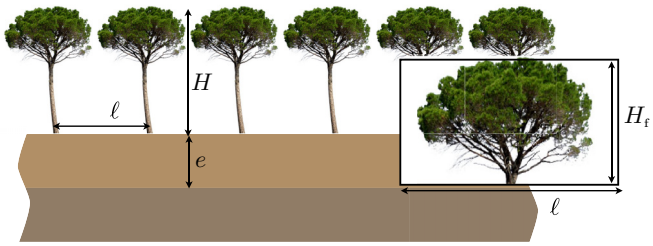

FIG. 1. Periodic array of trees with spacing ℓ and total height H; the ground region is surmounted by a guiding layer able to support Love waves. The tree trunks have a diameter d and filling fraction φ_t, and the foliage of height H_f has a surface filling fraction φ_f.

surface and we shall see that these surface waves are particularly sensitive to the shape of structural elements above the soil; in the present case, a forest of trees with some foliage (Fig. 1). The effective dispersion relation reflects a cooperation between the guiding layer and the trees, resulting in effective band gaps for a hybrid wave. As a result, it is shown that a forest of trees with varying height can reflect, localize, or convert a Love wave.

The paper is organized as follows. In Sec. II, the dispersion relations of the hybrid guided waves are derived in Eqs. (7) and (11) (in the absence and in the presence of foliage, respectively); the result is obtained owing to a homogenization procedure, which is detailed in Appendix A. The accuracy of the dispersion relations is inspected in Sec. III for a forest of constant height; afterwards they are used to interpret the numerical results for a wedge of trees with varying heights in Sec. IV. Section V analyzes the robustness of the wedge effect with respect to disorder in the height and in the positions of the trees and with respect to a three-dimensional effect. We give, in the appendices, further details of the asymptotic analysis as well as additional results including the numerical resolutions of the actual/homogenized problems and a discussion on mass-spring models used in [22–25].

II. MODELING

The propagation of elastodynamic waves in a heterogeneous isotropic medium is governed by the Navier equation,

$$\rho\frac{\partial^2\mathbf{u}}{\partial t^2} = \mathrm{div}\boldsymbol{\sigma}, \quad \boldsymbol{\sigma} = \mathbf{C} : \nabla\mathbf{u}, \tag{1}$$

with t the time variable. The body force is assumed to be zero, and $\mathbf{C} = (C_{ijkl})$ is the fourth-order elasticity tensor, which satisfies Hookes' law, $C_{ijkl} = \lambda\delta_{ij}\delta_{kl} + \mu(\delta_{ik}\delta_{jl} + \delta_{il}\delta_{jk})$, $i, j, k, l = 1, 2, 3$, where $\delta_{ij} = 1$ for $i = j$ and 0 otherwise. Moreover, λ and μ are the Lamé coefficients, ρ is the density, and $(\mathbf{u}, \boldsymbol{\sigma})$ are the vector displacement field and the second-order stress tensor, respectively. For an elastic medium which is invariant along one direction, say y, the Navier equation splits into an in-plane equation on $\mathbf{u} = (u_x, u_z)$ and an out-of-plane equation on $u = u_y$. We focus on the out-of-plane polarization which concerns Love waves. If one further assumes some time-harmonic dependence $e^{-i\omega t}$, with ω the angular wave frequency, this problem takes the simple form

$$\mathrm{div}\boldsymbol{\sigma} + \rho\omega^2 u = 0, \quad \boldsymbol{\sigma} = \mu\nabla u. \tag{2}$$

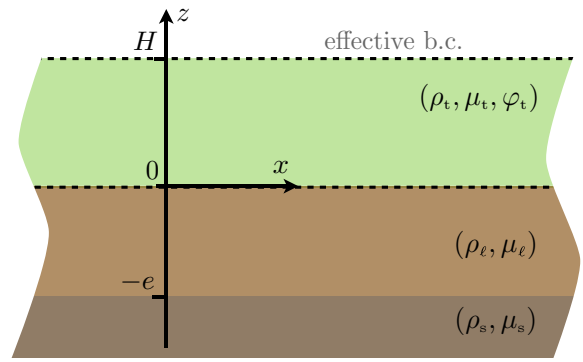

FIG. 2. The effective problem, in which the region of the trees $0 < z < H$ has been replaced by an equivalent (highly anisotropic) layer where the homogenized equation (3) applies, along with the continuities of u and σ_z at $z = -e$ and $z = 0$ and the boundary condition (4) at $z = H$.

We consider the two-dimensional configuration of a forest of trees periodically spaced by a distance ℓ; the ground is composed of a layer with a lower shear velocity than that of the soil substrate (Fig. 1). In the absence of trees, this low-velocity layer can support Love waves, which propagate within the layer and vanish when moving far from it in the substrate.

A. Homogenization of the tree region

From the viewpoint of the homogenization, a forest of trees is a structure of finite extent made of a stratified medium [26–28]. This structure can be homogenized using an asymptotic analysis in its bulk and at its boundaries and the procedure to do so is given in Appendix A. In the resulting effective problem depicted in Fig. 2, the region of the trees is replaced by an equivalent slab filled with a homogeneous anisotropic medium where $(u, \boldsymbol{\sigma})$ satisfy

$$\boldsymbol{\sigma} = \mu_t\begin{pmatrix}0 & 0\\ 0 & \varphi_t\end{pmatrix}\nabla u, \quad \mathrm{div}\boldsymbol{\sigma} + \rho_t\omega^2\varphi_t\, u = 0, \tag{3}$$

with (ρ_t, μ_t) the mass density and the shear modulus of the wood which compose the trees, and φ_t the filling fraction of tree trunks (denoting d the diameter of the trunk, $\varphi_t = d/\ell$). It is worth noting that (3) tells us that the propagation is allowed along the trees only, with the wave number ω/c_t, $c_t = \sqrt{\mu_t/\rho_t}$, as in a single tree [since (3) yields the wave equation $\partial_{zz}u + (\omega^2/c_t^2)\,u = 0$]. Next, effective boundary conditions apply at the interfaces of the effective slab at $z = 0$ and $z = H$. At the interface $z = 0$ with the guiding layer, the usual continuities of u and σ_z apply; at the interface $z = H$ with the air above the trees, a nonintuitive effective condition applies of the form

$$\sigma_z = -L_e\frac{\partial\sigma_z}{\partial z}, \quad L_e = H_f\left(\frac{\varphi_f}{\varphi_t}\frac{\rho_f}{\rho_t} - 1\right), \quad \text{at } z = H, \tag{4}$$

with (H_f, φ_f, ρ_f) the height, filling fraction, and mass density of the foliage (inset in Fig. 1). Eventually, the propagation is

described by (2) in the guiding layer, for $0 > z > -e$, with the material parameters (ρ_ℓ, μ_ℓ), and in the substrate, for $z < -e$, with the material parameters (ρ_s, μ_s).

The derivation of the effective condition (4) at the top of the trees, which is of the Robin's type, is detailed in Appendix A; see Eq. (A30). It is worth noting that in the absence of foliage, $H_f = 0$ and hence $L_e = 0$, so that the boundary condition at the top of the trees reduces to the usual stress-free boundary condition. We stress that the homogenization procedure can be conducted at higher order, resulting in nonintuitive transmission conditions at $z = 0$ appearing as a correction to the continuity relations that we use here. This is done in [27,28] but, in the present case, we checked that accounting for this higher-order correction does not significantly affect the results; hence it is disregarded. This would not be the case if heterogeneities, such as rocks or tree roots, were considered at the tree bottom.

B. Dispersion relations of the spoof Love waves

We start our analysis in the absence of foliage and, as previously said, (4) reduces in this case to $\sigma_{z|z=H} = 0$. Looking for a guided wave solution, which is the solution to the problem in the absence of source, we can derive the dispersion relation. Specifically, we are looking for solutions of the form

$$u(x,z) = \begin{cases} e^{\alpha_s(z+e)}e^{i\beta x}, & z < -e \\ [A\cos k_\ell z + B\sin k_\ell z]e^{i\beta x}, & -e < z < 0 \\ C\cos k_t(z-H)\, e^{i\beta x}, & 0 < z < H. \end{cases} \quad (5)$$

In (5), we have accounted for the condition $\sigma_{z|z=H} = 0$ and we have defined the vertical wave numbers

$$\alpha_s = \sqrt{\beta^2 - \frac{\omega^2}{c_s^2}}, \quad k_\ell = \sqrt{\frac{\omega^2}{c_\ell^2} - \beta^2}, \quad k_t = \frac{\omega}{c_t}, \quad (6)$$

and $c_a = \sqrt{\mu_a/\rho_a}$, $a = s, \ell, t$. Next, applying the continuity of u and σ_z at the interfaces at $z = -e$ and 0, (5) leaves us with four equations on (A, B, C, β) for each frequency ω, from which the dispersion relation $\beta(\omega)$ can be inferred. It reads as

$$1 - \frac{\mu_\ell k_\ell}{\mu_s \alpha_s}\tan k_\ell e - \frac{\mu_t k_t}{\mu_\ell k_\ell}\varphi_t \tan k_t H\left(\tan k_\ell e + \frac{\mu_\ell k_\ell}{\mu_s \alpha_s}\right) = 0. \quad (7)$$

In the above dispersion relation, α_s is real positive and β is real, which corresponds to a wave evanescent in the substrate $z < -e$, but k_ℓ can be *a priori* real or imaginary (k_t is real by definition). If k_ℓ is real, the wave is guided within the layer and the trees; if k_ℓ is imaginary, the wave is evanescent in the layer as it is in the ground, and hence the guiding effect is supported by the trees only.

It is worth noting that (7) simplifies in two limiting cases. Obviously, for $H = 0$, we recover the dispersion relation of Love waves,

$$\text{Love waves for } H = 0, \quad \alpha_s = \frac{\mu_\ell}{\mu_s} k_\ell \tan k_\ell e, \quad (8)$$

which are supported by the layer alone [18]. Conversely when $e = 0$, the trees alone are able to support guided waves, with

$$\text{elastic SPP for } e = 0, \quad \alpha_s = \frac{\mu_t}{\mu_s}\varphi_t k_t \tan k_t H; \quad (9)$$

in the case where $\mu_t = \mu_s$, we recover the dispersion relation of the so-called spoof plasmon corresponding in acoustics and electromagnetism to guided waves propagating over a rough rigid surface [2]. In between, the layer is coupled to the trees, resulting in a hybrid guided wave that we name "spoof Love wave."

Let us now move to the effect of the foliage. To do so, it is sufficient to modify in (5) the form of the solution for $0 < z < H$, specifically,

$$u(x,z) = C[\cos k_t(z-H) + k_t L_e \sin k_t(z-H)]e^{i\beta x}, \quad (10)$$

which satisfies (4), and the enriched dispersion relation is obtained in the form

$$F_1\left[1 - \frac{\mu_\ell k_\ell}{\mu_s \alpha_s}\tan k_\ell e\right] - F_2\,\frac{\mu_t k_t}{\mu_\ell k_\ell}\varphi_t\left(\tan k_\ell e + \frac{\mu_\ell k_\ell}{\mu_s \alpha_s}\right) = 0, \quad (11)$$

with

$$F_1 = 1 - k_t L_e \tan k_t H, \qquad F_2 = \tan k_t H + k_t L_e. \quad (12)$$

Obviously, in the absence of foliage, $L_e = 0$ and (11) simplifies into (7).

It is worth noting that the limiting case of the dispersion relation (8) of Love waves is exact, while that of the dispersion relation (9) of supporting spoof plasmons (SPPs) is an approximation valid for a wavelength larger than the array spacing ℓ, that is, $k\ell \ll 1$; we also stress that the validity of (9) is not limited in terms of kH values [26]. Next, although the dispersion relations (8) and (9) have a similar form, they correspond to guided waves of different nature and this is due to the definitions of k_ℓ and k_t in (6). The spectrum of Love waves is typical of waves guided in a waveguide: it is composed of different branches in the (β, ω) plane, all being comprised in the cone limited by the lines $\beta = \omega/c_s$ and $\beta = \omega/c_\ell$. The lowest branch starts at $\omega = 0$ and the following ones start at cut-on frequencies $\omega_n = n\omega_1$, $n = 0, 1, \ldots$, with

$$\omega_1 = \pi\frac{\delta c}{e} \quad \text{and} \quad \delta c = \frac{c_s c_\ell}{\sqrt{c_s^2 - c_\ell^2}}. \quad (13)$$

As such, above ω_n, $(n+1)$ guided waves can propagate. On the contrary, (9) has zero solution if $\tan(\omega H/c_t) < 0$ resulting in band gaps for $\omega \in [(2n-1)\omega_c, 2n\omega_c]$, $n = 1, 2, \ldots$, with

$$\omega_c = \pi\frac{c_t}{2H}, \quad (14)$$

and a unique solution otherwise, with an explicit dispersion relation $\beta(\omega) = \omega/c_s\sqrt{1 + A^2\tan^2(\omega H/c_t)}$ [$A = \varphi_t(\mu_t/\mu_s)(c_s/c_t)$] from (9). These two behaviors are illustrated in Fig. 3 where the dispersion relations have been calculated numerically in the actual configurations (arbitrary values of the material properties have been chosen). The validity of (9) is visible for $k_t H$ up to about 15, corresponding to $k_t\ell$ up to about 0.5 in the reported case. The numerical

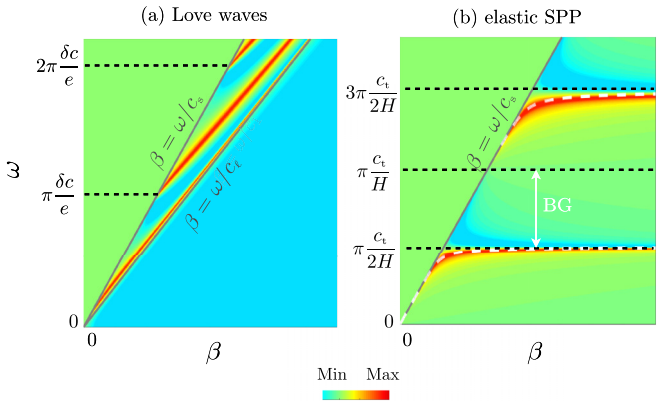

FIG. 3. Classical dispersion relations of (a) Love waves [Eq. (8)], with $\delta c = c_s c_\ell/\sqrt{c_s^2 - c_\ell^2}$ defining the cut-on frequencies $n\pi\delta c/e$, $n = 0, 1, \ldots$, and (b) elastic SPP exhibiting a band gap (BG) where guided waves cannot propagate, in the plane (β, ω). The dispersion relations are obtained numerically in the actual problems by means of the divergence of the reflection coefficient $|R|$ (in logarithmic color scale). Arbitrary scales have been used. In (b), dashed white lines show the dispersion relation (9).

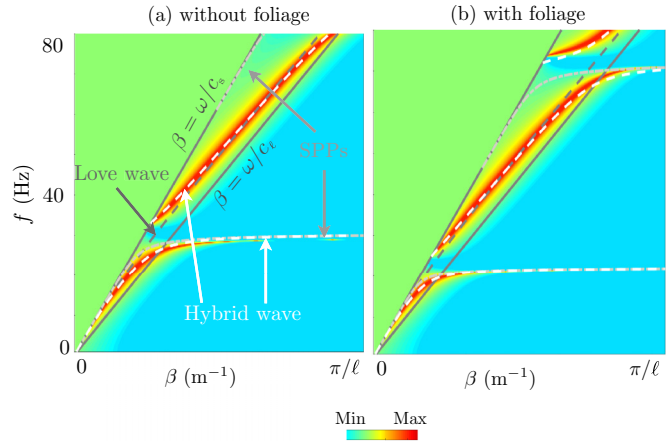

FIG. 4. Dispersion relation of the hybrid "spoof Love" wave for $H = 10$ m, calculated numerically (as in Fig. 3) and the dispersion relation (7) and (11) (dashed white lines). The hybrid wave results from a cooperation between the guiding layer supporting the Love wave (dashed dark-gray lines) and the trees supporting spoof plasmons (SPPs, light-gray lines); the light lines $\beta = \omega/c_s, \omega/c_\ell$ are reported in solid gray lines.

computation of the dispersion relations is done using a modal method based on eigenfunction expansions; see, e.g., [29]. It consists in computing the scattering coefficient, say the reflection coefficient R, for an incident wave in the substrate, and hence a solution for $z < -e$ of the form $u(x, z) = e^{i\beta x}(e^{-\alpha_s z} + Re^{\alpha_s z})$, with α_s in (6). Above the light line $\beta < \omega/c_s$, α_s is purely imaginary, whence $|R| = 1$ (the incident wave is propagating). Below the light line, α_s is purely real and $|R|$ is unbounded (the incident wave is evanescent); when $|R| = \infty$, we recover a guided wave as in (5).

III. VALIDATION OF THE MODEL

From now on, we use the following material parameters: $\rho_s = 1300$ kg m^{-3}, $c_s = 495$ m s^{-1} for the substrate, $\rho_\ell = 2600$ kg m^{-3}, $c_\ell = 350$ m s^{-1} for the guiding layer, and $\rho_t = 450$ kg m^{-3}, $c_t = 1200$ m s^{-1} for the tree. The dimensions are $e = 2$ m, $H = 10$ m, $d = 0.3$ m, $\ell = 2$ m ($\varphi_t = 0.15$). When the foliage is considered, we use $d_f = 1.5$ m ($\varphi_f = 0.75$) and $H_f = 1$ m; thus the height of the trunk is 9 m in this case and the same mass density is $\rho_f = \rho_t$ as for the trunk.

A. Band structure $\beta(f)$ of a forest with constant-height trees

To inspect the validity of our homogenized models, we computed numerically the dispersion relations in the actual problems, as for Fig. 3. Results on the reflection coefficient R are reported in Fig. 4 against β and the frequency f, and, for comparison, we also report the dispersion relation of the Love wave on its own and those of the spoof plasmons on their own. It is worth noting that with $\delta c \simeq 496$ m s^{-1}, the first cut-on frequency of Love waves appears at 120 Hz, well above the lower band gap of the elastic SPPs for $f \in (30, 60)$ Hz.

The actual dispersion relations confirm the coupling between the guiding layer and the trees resulting in a hybrid guided wave accurately described by our model (7) and (11) (dashed white lines). The behavior of the wave is close to that of the Love wave except in the vicinities of cutoff frequencies. There, the trees dominate and the wave becomes evanescent not only in the soil substrate but also in the guiding layer, with $\beta > \omega/c_\ell$. In the absence of foliage, the interpretation is easy. In the limit of large β (hence, $k_\ell \sim i\alpha_s$ and $\tan k_\ell e \sim i$), (7) simplifies into $\alpha_s \sim (\mu_t/\mu_\ell)\varphi_t k_t \tan k_t H$, which corresponds to a spoof plasmon (9) supported by the interface trees/guiding layer regardless of the presence of the substrate. It results that the first cutoff frequency visible at 30 Hz corresponds simply to (14). In the reported case, a band gap due to hybridization with the local resonance is opened within a small range of frequencies; it is worth noting that this band gap tends to disappear if the cutoff frequency ω_c in (14) approaches the first cut-on frequency of the Love waves, ω_1 in (13), as is the case in [25]. The scenario is the same in the presence of foliage, but the cutoff frequencies f_c in that case are significantly decreased in this case, a fact that is already true for the spoof plasmons in the absence of a guiding layer [$e = 0$ in (11)].

B. Dispersion relation $\beta(H)$ at $f = 30$ and 70 Hz

Here, we shall adopt a different perspective on the band structure reported in Fig. 4 for a fixed H; this will be useful in the sequel when a forest of trees with varying height will be considered. Instead of considering $\beta(f)$ for a fixed H, we consider $\beta(H)$ for a fixed frequency f. Figures 5 and 6 show the resulting dispersion relations with $H \in (2; 18)$ m at 30 and 70 Hz, respectively.

At 30 Hz, the lowest resonance of the trees without foliage occurs for $H \simeq 10$ m, from (14), resulting in a single band gap in Fig. 5(a) for $H \in (9.6, 10.8)$ m. With the foliage, the gap is shifted to $H \in (6.3, 7.5)$ m; see Fig. 5(b). At $f = 70$ Hz, the same trends in the dispersion relations are observed; see Fig. 6. With resonances taking place for trees of heights $H \simeq 4$ and 13 m, two band gaps for $H \in (3.5, 4)$

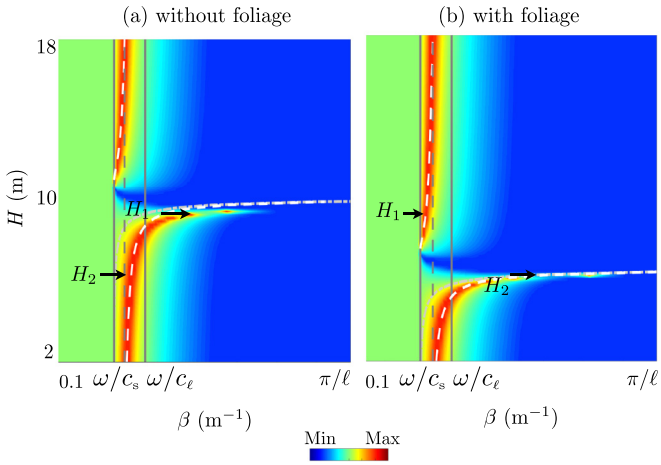

FIG. 5. Dispersion relation of the spoof Love waves in the plane (β, H) at $f = 30$ Hz (same representation as in Fig. 4 for dashed and solid lines). $\omega/c_s = 0.38$ m^{-1}, $\beta_{\text{Love}} = 0.49$ m^{-1}, $\omega/c_\ell = 0.54$ m^{-1}, $\pi/\ell = 1.57$m^{-1}. The band gaps are (a) (9.6,10.8) m and (b) (6.3,7.5) m.

m and $H \in (12.3, 13)$ m are now visible in the absence of foliage. As previously, the presence of the foliage produces a shift of the gaps, to $H \in (10, 10.5)$ m for the first one and to $H \in (1.5, 1.9)$ m for the second one.

It is worth noting that our model is accurate regardless of the height H of the trees and this is expected since the propagation within the trees is accounted for in the analysis. What is less expected is the robustness of the model with respect to the spacing ℓ ($k_t\ell = 0.3$–0.7) beyond the usual low-frequency regime; this robustness in homogenized models has been already observed in [27,28]. Eventually, and to complement the results on the dispersion relations, we report in Appendix B the shapes of the guiding waves in the vicinity of the band gaps ($H = H_1$ and H_2 in Figs. 5 and 6) in the actual and homogenized problems.

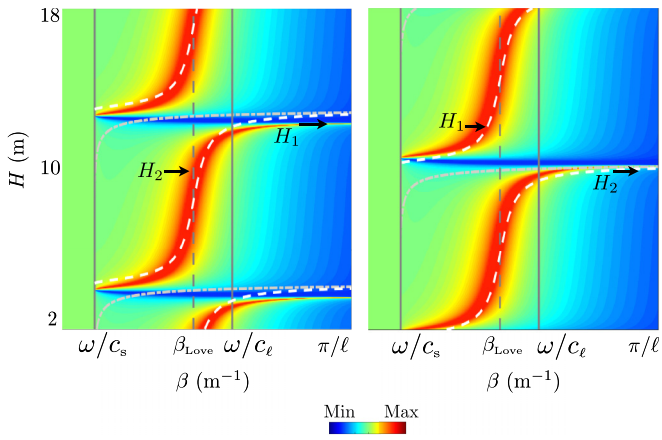

FIG. 6. Dispersion relation of the spoof Love waves in the plane (β, H) at $f = 70$ Hz; same representation as in Fig. 5. $\omega/c_s = 0.89$ m^{-1}, $\beta_{\text{Love}} = 1.15$ m^{-1}, $\omega/c_\ell = 1.25$ m^{-1}. The band gaps are (a) (3.5,4) m and (12.3,13) m, and (b) (10,10.5) m .

IV. TREES OF VARYING HEIGHTS, THE WEDGE EFFECT

We now move to the case of a forest of trees with increasing or decreasing heights. The forest is composed of trees whose height H varies from 2 to 16 m, with an increment of 0.5 m and with the same spacing $\ell = 2$ m as in the periodic case. The numerical computations are performed in the case of two-dimensional (2D) antiplane shear elasticity and in the time-harmonic regime using COMSOL MULTIPHYSICS; we consider a point source at 30 Hz and at 70 Hz outside the forest. We shall see that the coupling of the Love wave generated in the guiding layer by the source with the forest produces a hybrid wave whose behavior is strongly nonsymmetric depending on the position of the source on the shorter or on the taller edge of the forest, as has been already observed for Rayleigh waves [12,13]. Eventually, and following [7,12,13], we shall assume that the wave number β in a forest of trees with varying height $H(x)$ can be estimated locally by the wave number in a forest of the same but constant H; this is expected to be a reasonable approximation for small gradient of tree heights, in our case about 14°.

The results at 30 Hz are reported in Fig. 7. At this frequency, tree heights around 10 m (without foliage) and 7 m (with foliage) fall in band gaps where the spoof Love wave cannot propagate; see Fig. 5.

Let us start with the case where the source is located on the lower edge of the forest; see Figs. 7(a) and 7(b). In this case, the Love wave generated in the guiding layer is first converted into a hybrid spoof Love wave which propagates from right to left along trees with increasing height up to a "trapping" location where the wave stops. This is the analog to the acoustic rainbow [7] and, according to the local analysis, the mechanism is similar: from Fig. 5(a) in the absence of foliage, the wave propagating from shorter $H < 10$ m towards higher trees has a local wave number $\beta(H)$ increasing along the branch $\beta(H < 10$ m). Eventually, it reaches the value π/ℓ at the lower edge of the band gap, where the confinement in the trees is maximum; notably, the wave is evanescent in the guiding layer as it is in the substrate. Due to the strong dispersion at this lower edge, it progressively slows down up to an almost vanishing group velocity, which results in a localized energy concentration, as reported in [30]. This is expected at a tree height $H = 9.6$ m from Fig. 5(a) without foliage, and at $H = 6.3$ m from Fig. 5(b) with foliage, and this conforms with the observations in Figs. 7(a) and 7(b).

We now consider the case where the source is located on the taller edge of the forest; see Figs. 7(c) and 7(d). The Love wave enters the forest where it is converted first in a hybrid wave propagating from left to right up to a "turning point" where it is then converted in a bulk shear wave propagating downward into the substrate. This is the analog of the conversion of the Rayleigh wave reported in [12,13] and the local analysis is again helpful to interpret this feature. In the absence of foliage, the local wave number $\beta(H)$ of the hybrid wave now follows the branch $\beta(H > 10$ m) in Fig. 5(a); accordingly, the local wave number decreases from a value higher than that of the Love wave to a smaller one. Eventually, at the upper edge of the band gap, it reaches that of the bulk shear wave $\beta_s = \omega/c_s$ where the confinement

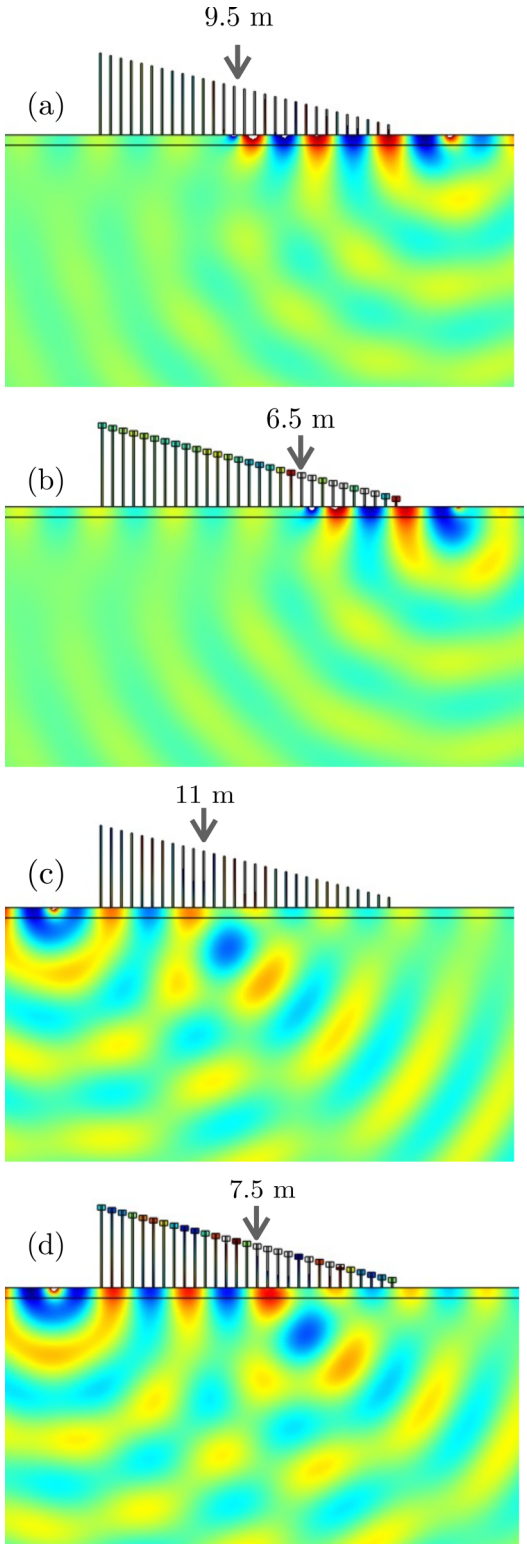

FIG. 7. (a),(b) Reflection and (c),(d) conversion of a Love wave of frequency $f = 30$ Hz by a forest consisting of 29 trees with heights varying from 16 to 2 m. The linear color range is in arbitrary units (white color is out of scale).

vanishes [$\alpha_s = 0$ in (6)]. Following this scenario, it seems not too hazardous to state that when propagating along trees with decreasing height, the wave becomes more and more adapted

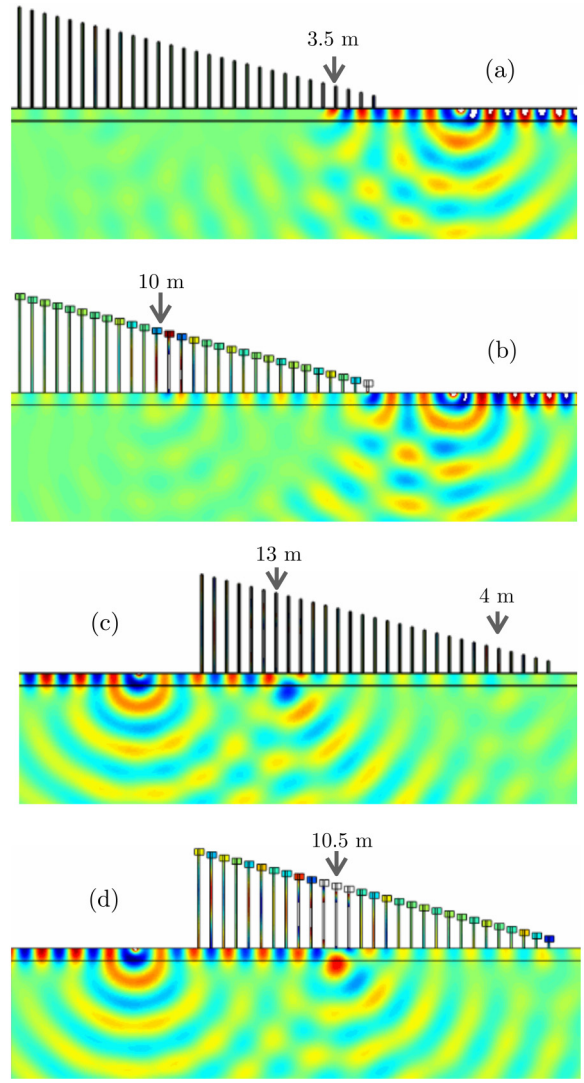

FIG. 8. (a),(b) Reflection and (c),(d) conversion of a Love wave of frequency $f = 70$ Hz; same representation as in Fig. 7.

to be converted into a shear wave in the bulk. The turning points observed in Figs. 7(c) and 7(d) coincide well with the upper limits of the band gaps reported in Fig. 5 (10.8 and 7.5 m without and with foliage, respectively).

Similar mechanisms of wave trapping and of wave conversion are observed at 70 Hz. Results are reported in Fig. 8, with some specific features that we comment on now. In the absence of foliage, two trapping points are possible for $H = 3.5$ m and $H = 12.3$ m from Fig. 6(a), but the trapping effect is visible at the first location $H = 3.5$ m only where the wave is already almost completely stopped. In the presence of foliage, the trapping point expected at $H = 10$ m from Fig. 6(b) is visible (notably the wave amplitude within the trees is high at this location), but what is more visible is the important reflection of the incident Love wave when it encounters the forest. This poor coupling is attributable to the vicinity of the band gap for $H \in (1.5, 1.9)$ m which results in a mismatch in the wave numbers of the incident Love wave, $\beta_{\text{Love}} = 1.15\ \text{m}^{-1}$, and the wave number of the spoof Love wave, $\beta(H = 2\ \text{m}) = 0.9\ \text{m}^{-1}$. In comparison, $\beta(H = 2\ \text{m})$

$= 1.18\ \mathrm{m}^{-1}$ in the absence of foliage, resulting in an efficient coupling in Fig. 8(a). Next, the conversion into a bulk shear wave is visible in Fig. 8(c) (the forest without foliage) at a turning point for $H \simeq 13$ m, in agreement with the value of the upper edge of the first band gap encountered for decreasing H in Fig. 6(a). The second turning point expected at $H = 4$ m is also visible although the amplitude of the guided wave has decreased significantly because of the primary wave conversion.

Eventually, it can be seen from Figs. 7(c) and 7(d) and Figs. 8(c) and 8(d) that after the wave conversion at the turning points, the shear wave propagates in the substrate with a rather well-defined direction, a fact already observed for Rayleigh waves [12,13]. It is observed that the corresponding refraction angle decreases (with respect to the horizontal direction) in the presence of foliage. At 30 Hz, the decrease is small, from about 38° to 36° (with and without foliage); at 70 Hz, it is more significant, from about 47° to 38°. Our homogenized model does not provide a theoretical value of this angle. Indeed, the problem of a Love wave interacting with a wedge in which (3) applies is rather simple, but it has to be solved numerically. It is shown in Appendix B that doing so provides a realistic picture of the wedge effect, which shows that the homogenized problem contains all the ingredients necessary to describe the mechanism of wave conversion.

At that point, we have shown that the local analysis carried out for trees of constant height works equally well for trees of varying height. It remains for us to inspect whether or not this analysis is robust when moving toward more realistic configurations, namely, to inspect the effect of inherent disorders in the tree distribution and the robustness of the mechanism captured by our two-dimensional model in three dimensions. We address these issues in the next section.

V. ROBUSTNESS OF THE MECHANISM OF WAVE CONVERSION WITH RESPECT TO DISORDER AND 3D EFFECT

In this section, we restrict ourselves to a forest of trees without foliage and we focus on the mechanism of wave conversion, with a source located near the taller edge of the forest. The details of the numerical implementation of the 3D problem with COMSOL are given in Appendix D. Eventually, to avoid lengthy computations, the effect of the disorder is inspected in a 2D setting and the 3D effect is inspected in a perfect periodic forest.

A. Persistence of the wave conversion in the presence of disorder

We start by inspecting the effect of disorders in the tree heights and in their locations; this corresponds to classical disorders say in the strength and in the position of scatterers for multiple scattering problems. To do so, we consider the reference case as in the preceding section with trees of height $H \in (2, 16)$ m periodically located with spacing $\ell = 2$ m and of constant height increment of 0.5 m. The fields in Figs. 9(a) and 10(a) simply reproduce that of Figs. 7(a) and 8(a) as the benchmarks.

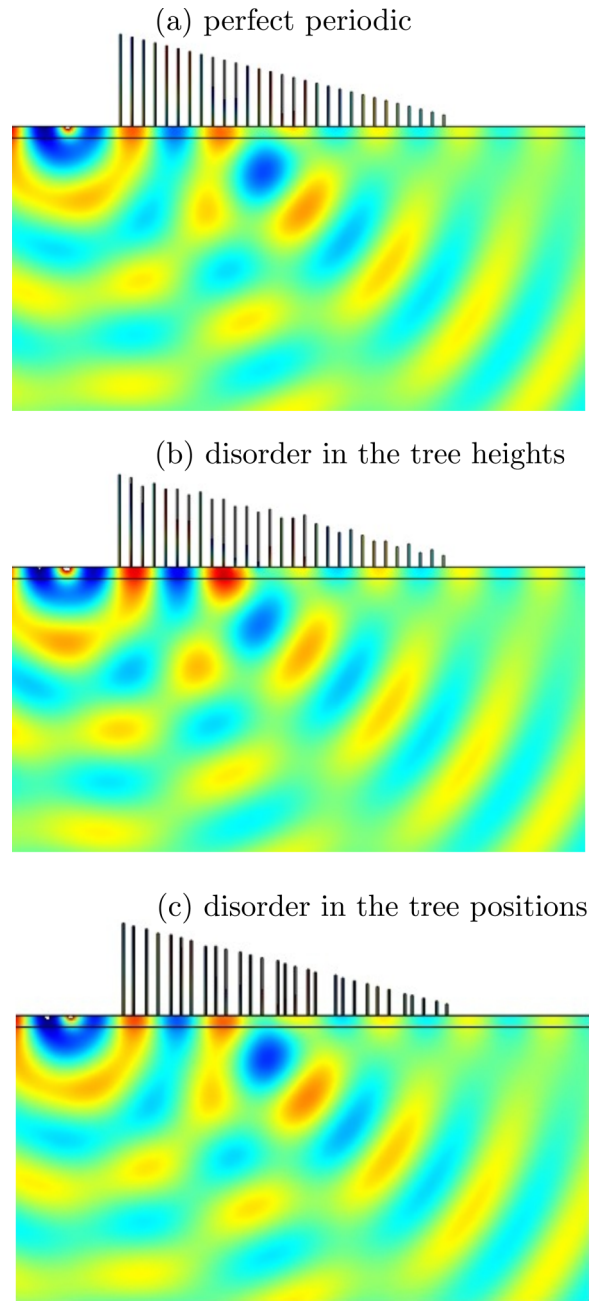

FIG. 9. Conversion of a Love wave of frequency $f = 30$ Hz with a forest as in Fig. 7(a). (b) Same as (a) for trees with perturb height. (c) Same as (a) for trees with perturb position. The linear color range is in arbitrary units (white color is out of scale).

Next, we keep the same tree locations and allow for random variations in each tree height with maximum amplitude of $H/10$, resulting in the fields of Figs. 9(b) and 10(b). Eventually, we allow for variations in the tree positions around their periodic position with a maximum displacement of $\ell/5$. This is done while keeping the same slope, hence interrogating the disorder in position only. Typical realizations are shown in Figs. 9(c) and 10(c). Note that this latter disorder is the most classical and it is admitted that within effective medium approaches, it is not essential that the arrangement of scatterers is periodic or random; see, e.g., [31].

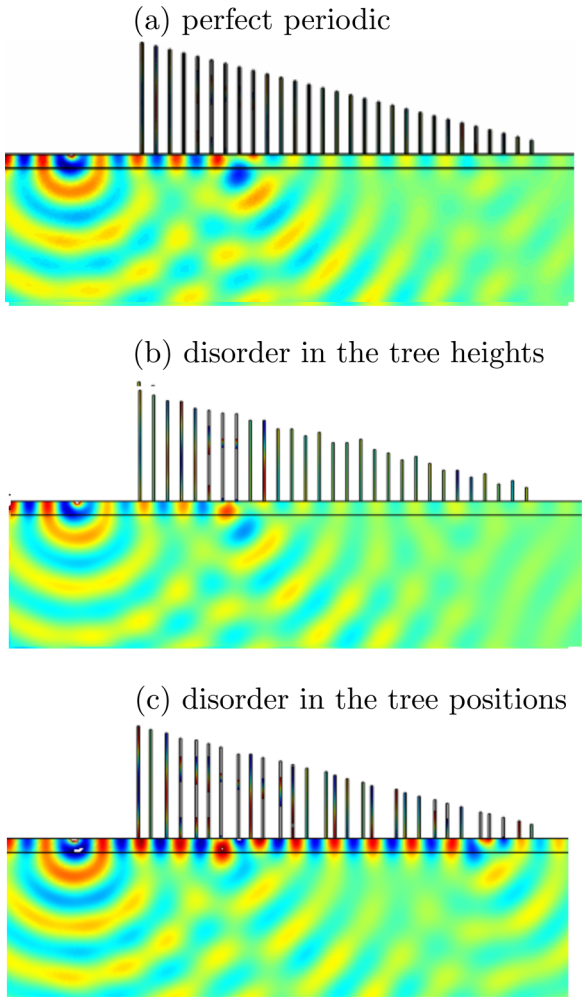

FIG. 10. Same representation as in Fig. 9 for $f = 70$ Hz.

At the lowest frequency $f = 30$ Hz, the variations in the wave patterns induced by the two types of disorder are incidental and the main features observed for the perfect periodic case are fully recovered. In particular, the turning points and the angle of refraction of the shear wave in the bulk remain identical.

Expectedly, the variations in the patterns are more pronounced at $f = 70$ Hz. The guided wave having a shorter wavelength becomes more sensitive to any defect in the tree arrangement. This sensitivity is particularly visible in the case reported in Fig. 10(c). There, a relatively large variation of the spacing takes place at the expected turning point for $H \sim 13$ m; as a result, the first wave conversion is significantly reduced which makes the second wave conversion (for $H \sim 4$ m) more visible.

B. Persistence of the wave conversion in a three-dimensional setting

We now move a step closer to a real forest, namely, cylindrical trees in three dimensions. We consider the following configuration: each tree has a square cross section of 0.09 m^2 and the array has the same spacing of 2 m along x and y; the array is composed of 23 $\times$ 14 trees along x and y, respectively

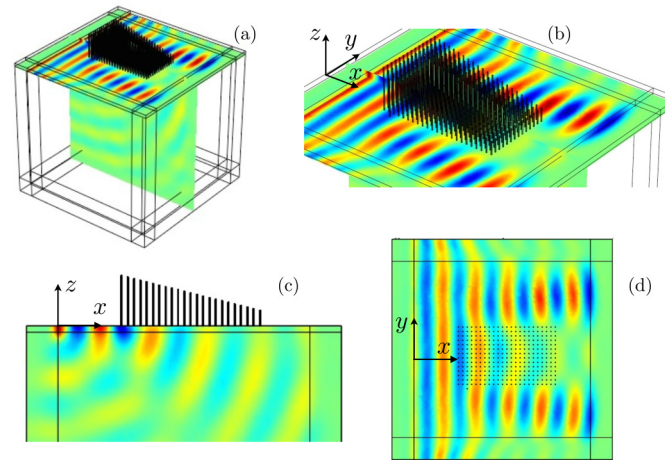

FIG. 11. Interaction of a Love wave of frequency $f = 30$ Hz with a three-dimensional forest consisting of 322 trees equally spaced along x and y, with heights varying from 16 to 2 m. (a) 3D plot of real part of the displacement u_y along y. (b) Zoom-in of u_y in (a). (c) Slice of u_y in the (x, z) plane corresponding to the 2D plot in Fig. 7(a). (d) Slice of u_y in the (y, z) plane revealing 3D effects by means of wave-front distortion. The linear color range is in arbitrary units.

(hence 322 trees); each row along y is composed of trees of the same height and along x the tree height decreases from 16 to 2 m with constant decrement. In the numerics, whose details are collected in Appendix D, we considered the full elastodynamic wave equations (1) in the time-harmonic regime and we used a source in the form of an incident-plane Love wave along y. It is worth noting that the geometry of the forest being not invariant along the y direction, the propagation involves both shear and longitudinal waves *a priori*, which may appear by conversion of the incident polarized Love wave. We estimated the importance of the mode conversions by calculating the averages of $|\mathbf{u} \cdot \mathbf{e}_a|^2/|\mathbf{u} \cdot \mathbf{e}_y|^2$, $a = x, z$, in the vertical plane passing through the forest. With 8% and 6% as results, it appears that the wave essentially keeps the same polarization when it propagates.

Different views of the pattern of the horizontal displacement u (along z) at 30 Hz are reported in Figs. 11. The shielding effect of the forest is clearly visible in Figs. 11(a) and 11(b), with the Love wave unable to emerge from the forest while propagating around it in the x direction. Next, Fig. 11(c) reports a vertical cut of the field in the (x, z) plane in the middle of the forest. Following the same scenario as in 2D, the Love wave first couples to the forest and propagates through the trees with decreasing heights; eventually, when it encounters a tree of height about 13 m, it is converted into a bulk shear wave. A noticeable difference with the 2D case is that the angle of refraction of the wave in the bulk is significantly lower here, about 20° versus 38° in 2D; see, also, Fig. 7(a). This is attributable to the shape of the trees, i.e., cylinders instead of walls in 2D, which produce flexural beam modes rather than antiplane shear plate modes. Hence, the coupling of Love waves with the trees and the conversion into shear bulk wave are confirmed, but the extension of the 2D calculation to the 3D case remains to be done to capture the physics of the beam flexion.

VI. CONCLUDING REMARKS

In this study, we have reported direct numerical observations of out-of-plane shear surface waves propagating in a forest of trees atop a guiding layer. Analytical dispersion relation obtained in closed form thanks to asymptotic expansions shows that this wave shares common features with both Love waves and spoof plasmons, which are recovered as limiting cases (trees of vanishing height, and guiding layer of vanishing thickness, respectively), hence the nickname "spoof Love wave." In the general case where the propagation is dictated by the coupling between the guiding layer and the forest, it reveals band gaps opened due to hybridization of Love waves with the local resonances of a single tree. This finding shows that spoof Love waves propagate following the same scenario as that already reported for Rayleigh waves. When propagating in a forest with decreasing tree height, they are easily converted into a downward bulk wave, while when propagating in a forest with increasing tree height, they slow down, being eventually trapped within the trees, as in the rainbow effect. Finally, we have shown that the presence of foliage significantly affects the local resonances of the trees, and hence the whole dispersion relation, a phenomenon which is neatly captured by our model.

Our model concerns an idealized two-dimensional and perfectly periodic setting. We have shown that the conversion of waves is hardly affected by disorder in the height or in the positions of trees at low frequency, and that the mechanism is preserved in a three-dimensional setting. In this latter case, however, the quantitative features of the wave conversion differ due to the appearance of flexural modes of the rods (cylindrical trees). Natural extensions of the present study concern (1) three-dimensional effect to quantitatively account for flexural modes at low frequencies and coupling of flexural and longitudinal modes at higher frequencies, (2) more realistic effects in the composition of the soil as material properties, e.g., viscoelasticity or vertical gradients of mass density, and (3) presence of heterogeneities, e.g., accounting for tree roots or rocks. Another aspect kept aside is asymptotic analysis of nonlinear effects which might arise in very soft soils.

ACKNOWLEDGMENTS

A.M. thanks the support of LABEX WIFI (Laboratory of Excellence within the French Program "Invest- ments for the Future") under references ANR-10-LABX-24 and ANR-10-IDEX-0001-02 PSL*.

APPENDIX A: THE HOMOGENIZED MODEL

In this appendix, we give a comprehensive derivation of the effective model for the forest of trees, which uses mathematical techniques developed in [27,28].

In the asymptotic analysis that we shall conduct, we use the macroscopic (usual) coordinate $\mathbf{x} = (x, z)$ and we introduce the microscopic coordinate $\boldsymbol{\chi} = (\chi, \zeta)$, with

$$\boldsymbol{\chi} = \frac{\mathbf{x}}{\ell}, \tag{A1}$$

with $\ell = \varepsilon$ the small parameter (where small means "small compared to the typical wave number"). Further, $\mathbf{e}_x = (1, 0)$ and $\mathbf{e}_z = (0, 1)$ denote the vectors of the canonical basis. In what follows, we focus our analysis on a so-called antiplane shear problem, posed in the (x, z) plane, and we shall establish the effective problem on $(u^e, \boldsymbol{\sigma}^e)$, which reads as

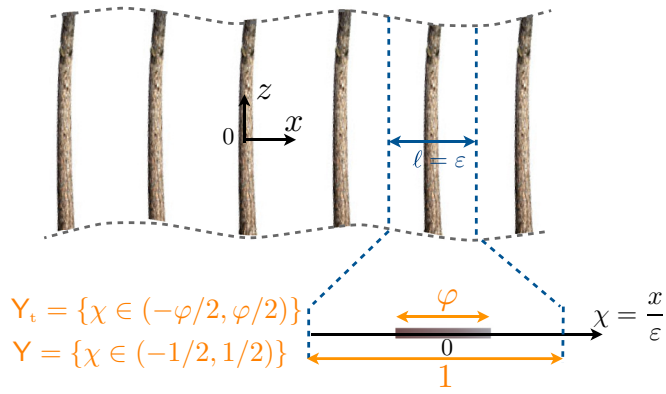

FIG. 12. Homogenization in the bulk of the tree forest, far from the top and the bottom of the trees. In the $\mathbf{x} = (x, z)$ coordinate, the array has a spacing $\varepsilon = \ell$ (the trees are assumed to be invariant along z). The rescaling in the horizontal $\chi = x/\varepsilon$ coordinate is shown in the inset.

$$\begin{aligned}
\boldsymbol{\sigma}^e &= \mu_t \begin{pmatrix} 0 & 0 \\ 0 & \varphi_t \end{pmatrix} \nabla u^e, \\
\boldsymbol{\sigma}^e + \rho_t \omega^2 \varphi_t \, u^e &= 0 \quad \text{for} \quad 0 < z < H, \\
\sigma_z^e &= -H_f \left(\frac{\varphi_f}{\varphi_t} \frac{\rho_f}{\rho_t} - 1 \right) \frac{\partial \sigma_z^e}{\partial z} \quad \text{at } z = H, \\
u^e(x, 0^+) &= u^e(x, 0^-), \quad \sigma_z^e(x, 0^+) = \sigma_z^e(x, 0^-),
\end{aligned} \tag{A2}$$

and $(u^e, \boldsymbol{\sigma}^e)$ admit the same expansions as $(u, \boldsymbol{\sigma})$ up to $O(\varepsilon^2)$.

1. The homogenized wave equation

The homogenized wave equation has to be derived in the region of the trees, $z \in (0, H)$, and therein the asymptotic analysis will be conducted using expansions of the fields with respect to the small parameter ε. The equations in the bulk of each tree are established far from the interface (air/tree) and far from the top of the trees, which is when the boundary-layer effects are disregarded. In this region, the fields vary over long distances, across many trees with x, and in the vertical direction along the trees with z. Once this macroscopic displacement has been defined by $\mathbf{x}$, we describe the microscopic horizontal displacement inside a single tree with χ. Note that ζ (the microscopic vertical displacement) is not needed since the trees are assumed to be invariant along z (Fig. 12).
Thus the rescaled differential operator reads as

$$\nabla \to \frac{\boldsymbol{e}_x}{\varepsilon} \frac{\partial}{\partial \chi} + \nabla_{\mathbf{x}}, \tag{A3}$$

which is used in the equations

$$\boldsymbol{\sigma} = \mu_t \nabla u, \quad \text{div}\boldsymbol{\sigma} + \rho_t \omega^2 \, u = 0, \tag{A4}$$

owing to the expansions

$$\begin{aligned}
u &= u^0(\mathbf{x}, \chi) + \varepsilon u^1(\mathbf{x}, \chi) + \cdots, \\
\boldsymbol{\sigma} &= \boldsymbol{\sigma}^0(\mathbf{x}, \chi) + \varepsilon \boldsymbol{\sigma}^1(\mathbf{x}, \chi) + \cdots,
\end{aligned} \tag{A5}$$

and χ is bounded in $\mathsf{Y}_\mathrm{t} = \{\chi \in (-\varphi_\mathrm{t}/2, \varphi_\mathrm{t}/2)\}$. It is worth noting that contrary to the cases where the unit cell is filled with some material, whence $\chi \in (-1/2, 1/2)$, here we are in a case where the boundaries at $\chi = \pm 1/2$ are not questioned. However, since we want to ensure the equilibrium of the force in the homogenized problem, we shall establish the equations satisfied by the effective fields $\langle u^n \rangle$ and $\langle \boldsymbol{\sigma}^n \rangle$, $n = 0, 1$, where we defined

$$\langle u^n \rangle(\mathbf{x}) \equiv \frac{1}{\varphi_\mathrm{t}} \int_{\mathsf{Y}_\mathrm{t}} u^n(\mathbf{x}, \chi) d\chi, \quad \langle \boldsymbol{\sigma}^n \rangle(\mathbf{x}) \equiv \int_{\mathsf{Y}_\mathrm{t}} \boldsymbol{\sigma}^n(\mathbf{x}, \chi) d\chi. \tag{A6}$$

Doing so, we implicitly assume that the stress tensor has been extended by 0 in $\mathsf{Y}\backslash\mathsf{Y}_\mathrm{t}$, with $\mathsf{Y} = \{\chi \in (-1/2, 1/2)\}$. At the leading order in $1/\varepsilon$, we get

$$\frac{\partial u^0}{\partial \chi} = \frac{\partial \sigma_x^0}{\partial \chi} = 0, \tag{A7}$$

which tells us that $u^0(\mathbf{x})$ and $\sigma_x^0(\mathbf{x})$ do not depend on χ. It follows that σ_x^0 is constant in Y_t and, as it vanishes at the interface air/tree $\chi = \pm\varphi_\mathrm{t}/2$, it is zero everywhere in Y_t. Thus we have

$$\sigma_x^0 = 0, \quad u^0(\mathbf{x}). \tag{A8}$$

At the order ε^0, we also have, in Y_t,

$$\sigma_z^0(\mathbf{x}) = \mu_\mathrm{t} \frac{\partial u^0}{\partial z}(\mathbf{x}),$$
$$\frac{\partial \sigma_z^0}{\partial z}(\mathbf{x}) + \frac{\partial \sigma_x^1}{\partial \chi}(\mathbf{x}, \chi) + \rho_\mathrm{t}\omega^2 u^0(\mathbf{x}) = 0, \tag{A9}$$

which, after integration over Y_t and accounting for $\sigma_x^1 = 0$ on the interface air/tree, leaves us with

$$\langle \sigma_z^0 \rangle(\mathbf{x}) = \mu_\mathrm{t}\varphi_\mathrm{t} \frac{\partial u^0}{\partial z}(\mathbf{x}),$$
$$\frac{\partial \langle \sigma_z^0 \rangle}{\partial z}(\mathbf{x}) + \rho_\mathrm{t}\omega^2 \varphi_\mathrm{t} u^0(\mathbf{x}) = 0. \tag{A10}$$

We now move to the next order. Since (A9) and (A10) hold in Y_t with $\langle \sigma_z^0 \rangle = \varphi_\mathrm{t}\sigma_z^0$, we deduce that σ_x^1 is independent of χ; thus, as σ_x^0, it is zero in Y_t. Owing to the relation $0 = \sigma_x^0 = \mu_\mathrm{t}[\partial_x u^0(\mathbf{x}) + \partial_\chi u^1(\mathbf{x}, \chi)]$, we also have

$$u^1(\mathbf{x}, \chi) = -\chi \frac{\partial u^0}{\partial x}(\mathbf{x}) + \langle u^1 \rangle(\mathbf{x}), \quad \text{in } \mathsf{Y}_\mathrm{t}, \tag{A11}$$

with the origin of χ chosen such that $\langle \chi \rangle = 0$. It follows that

$$\sigma_z^1(\mathbf{x}, \chi) = \mu_\mathrm{t} \frac{\partial u^1}{\partial z}(\mathbf{x}, \chi) = \mu_\mathrm{t} \left[-\chi \frac{\partial^2 u^0}{\partial z \partial x}(\mathbf{x}) + \frac{\partial \langle u^1 \rangle}{\partial z}(\mathbf{x}) \right], \tag{A12}$$

which, after integration over Y_t and thanks to $\langle \chi \rangle = 0$, leaves us with

$$\langle \sigma_z^1 \rangle(\mathbf{x}) = \mu_\mathrm{t}\varphi_\mathrm{t} \frac{\partial \langle u^1 \rangle}{\partial z}(\mathbf{x}). \tag{A13}$$

Eventually, the equation of equilibrium at the order ε reads as

$$\mathrm{div}_\mathbf{x} \boldsymbol{\sigma}^1 + \frac{\partial \sigma_x^2}{\partial \chi} + \rho_\mathrm{t}\omega^2 u^1 = 0, \quad \text{in } \mathsf{Y}_\mathrm{t}, \tag{A14}$$

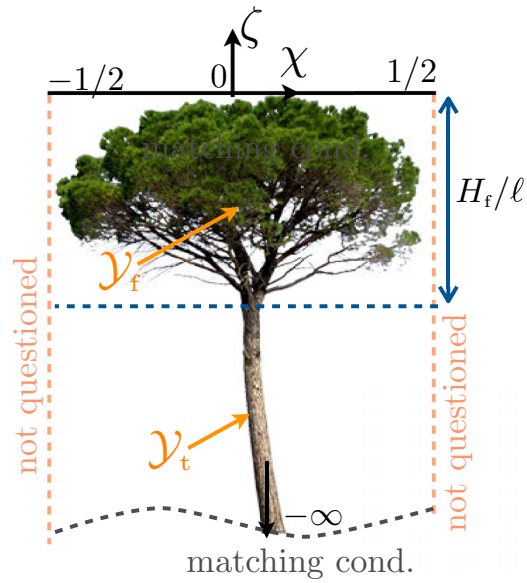

FIG. 13. Unit cell at the top of the trees in $\boldsymbol{\chi} = (\zeta, \chi)$ coordinate. $\mathcal{Y}_\mathrm{t}$ is the region of the tree for $\chi \in (-\varphi_\mathrm{t}/2, \varphi_\mathrm{t}/2)$ and $\zeta \in (-\infty, -H_\mathrm{f}/\ell)$, and $\mathcal{Y}_\mathrm{f}$ is the region of the foliage bounded in $(-1/2, 1/2) \times (-H_\mathrm{f}/\ell, 0)$ and of surface $|\mathcal{Y}_\mathrm{f}|$; φ_f is the filling fraction of foliage such that $|\mathcal{Y}_\mathrm{f}| = \varphi_\mathrm{f} H_\mathrm{f}/\ell$.

which after integration over Y_t provides us with

$$\frac{\partial \langle \sigma_z^1 \rangle}{\partial z}(\mathbf{x}) + \rho_\mathrm{t}\omega^2 \varphi_\mathrm{t} \langle u^1 \rangle(\mathbf{x}) = 0. \tag{A15}$$

2. Effective boundary condition at top of trees

The homogenized wave equation derived above has to be supplied with boundary conditions when approaching the top of the trees at $z = H$. To do so, we define an inner region which possibly contains a foliage. In this region, the vertical displacement in z is limited to a region of typical extent ℓ with rapid variations of the fields. These rapid variations are accounted for by defining the microscopic coordinate

$$\zeta = \frac{z - H}{\varepsilon}, \tag{A16}$$

whose origin is at the top of the foliage, in addition to χ. Eventually, the horizontal long-distance variations of the fields across the trees are captured by keeping x as an additional coordinate. Accordingly, we consider the following asymptotic expansions:

$$\begin{aligned} u &= v^0(x, \boldsymbol{\chi}) + \varepsilon v^1(x, \boldsymbol{\chi}) + \cdots, \\ \boldsymbol{\sigma} &= \boldsymbol{\tau}^0(x, \boldsymbol{\chi}) + \varepsilon \boldsymbol{\tau}^1(x, \boldsymbol{\chi}) + \cdots, \end{aligned} \tag{A17}$$

with $\boldsymbol{\chi} \in \mathcal{Y}$, and $\mathcal{Y} = \mathcal{Y}_\mathrm{f} \cup \mathcal{Y}_\mathrm{t}$, where $\mathcal{Y}_\mathrm{f}$ refers to a region of small extent H_f (vertically) containing the foliage, and small means "of the order of ℓ" (remember that $\varepsilon = \ell$); see Fig. 13.

In this region, one can account for a complex foliage using

$$\boldsymbol{\sigma} = \mu(\boldsymbol{\chi}) \nabla u, \quad \mathrm{div}\boldsymbol{\sigma} + \rho(\boldsymbol{\chi})\omega^2 u = 0, \tag{A18}$$

with $[\mu(\boldsymbol{\chi}), \rho(\boldsymbol{\chi})]$ able to describe variations in the material properties of the foliage with respect to the tree, and also variations of the material properties within the foliage. The

above equations need to be supplied with boundary conditions, which are of the Neumann type at the boundaries of the tree and of the foliage with the air, and the continuities of the displacement and of the normal stress at each discontinuity in the material properties (e.g., between the tree and the foliage). Eventually, the fields described by the expansions (A17) which hold in the vicinity of the top of the trees (including the foliage) have to match those defined in (A5) which hold far from the top of the trees. This is written in an intermediate region where $z \to H$ and $\zeta \to -\infty$ using $(z - H) = \varepsilon\zeta$ in (A5) and reexpanding. We get the so-called matching conditions at the first and second orders, which read as

$$\lim_{\zeta\to-\infty} v^0(x,\boldsymbol{\chi}) = u^0(x,H),$$
$$\lim_{\zeta\to-\infty} \boldsymbol{\tau}^0(x,\boldsymbol{\chi}) = \boldsymbol{\sigma}^0(x,H,\chi), \tag{A19}$$
$$\lim_{\zeta\to-\infty} v^1(x,\boldsymbol{\chi}) = u^1(x,H,\chi) + \zeta\frac{\partial u^0}{\partial z}(x,H),$$
$$\lim_{\zeta\to-\infty} \boldsymbol{\tau}^1(x,\boldsymbol{\chi}) = \boldsymbol{\sigma}^1(x,H,\chi) + \zeta\frac{\partial \boldsymbol{\sigma}^0}{\partial z}(x,H,\chi). \tag{A20}$$

These matching conditions are obtained as additional boundary conditions for the two problems on $(u,\boldsymbol{\sigma})$ and $(v,\boldsymbol{\tau})$. Both have to coincide in some intermediate region, where the evanescent field encapsulated in $(v,\boldsymbol{\tau})$ is vanishing for large ζ and hence only the behavior of the propagating field remains. The matching conditions are written setting $u^0 + \varepsilon u^1 + \cdots \sim v^0 + \varepsilon v^1 + \cdots$ in this intermediate region of typical extent, say, $x_1 = O(\sqrt{\varepsilon}) \to 0$ and $y_1 = O(1/\sqrt{\varepsilon}) \to \infty$. Next, using Taylor expansions of $u^0(x,z) = u^0(x,H) + \varepsilon\zeta\partial_z u^0(x,H) + \cdots$, the same for $\boldsymbol{\sigma}^0$, and identifying the terms in ε^n, $n = 0, 1, \ldots$ of the two expansions provides (A19) and (A20) for $n = 0, 1$. In this region, the differential operator reads as

$$\boldsymbol{\nabla} \to \boldsymbol{e}_x\frac{\partial}{\partial x} + \frac{1}{\varepsilon}\boldsymbol{\nabla}_{\boldsymbol{\chi}}. \tag{A21}$$

At the leading order, we have $\mathrm{div}_{\boldsymbol{\chi}}\boldsymbol{\tau}^0 = 0$, which after integration over $\mathcal{Y}$ and accounting for the boundary conditions and the matching condition on $\boldsymbol{\tau}^0$ leaves us with

$$0 = \lim_{\zeta\to-\infty}\int_{\mathsf{Y}_\mathrm{t}} \tau_z^0(x,\boldsymbol{\chi})d\chi = \sigma_z^0(x,H), \tag{A22}$$

from which the boundary condition at the leading order is the usual stress-free condition, regardless of the presence of the foliage. To capture this effect, we have to move to the next order. At the next order, we start with $\boldsymbol{\nabla}_{\boldsymbol{\chi}}v^0$, which tells us that

$$v^0(x) = u^0(x,H), \tag{A23}$$

thanks to the matching condition on v^0. This allows us to define the problem on $(\boldsymbol{\tau}^0, v^1)$, which reads as

$$\mathrm{div}_{\boldsymbol{\chi}}\boldsymbol{\tau}^0 = 0,$$
$$\boldsymbol{\tau}^0(x,\boldsymbol{\chi}) = \mu(\boldsymbol{\chi})\left[\frac{\partial u^0}{\partial x}(x,H)\boldsymbol{e}_x + \boldsymbol{\nabla}_{\boldsymbol{\chi}}v^1(x,\boldsymbol{\chi})\right],$$
$$\boldsymbol{\tau}^0\cdot\boldsymbol{n} = 0 \quad \text{on the interfaces with the air},$$
$$\lim_{\zeta\to-\infty}\boldsymbol{\tau}^0 = \boldsymbol{\sigma}^0(x,H,\chi) = \boldsymbol{0}, \tag{A24}$$

and where x appears as a parameter. For the limit $\zeta \to -\infty$, we used that $\sigma_x^0 = 0$ from the previous section and that $\sigma_z^0(x,H) = 0$ from (A22). The above system has an explicit solution of the form

$$\boldsymbol{\tau}^0 = 0, \quad v^1(x,\boldsymbol{\chi}) = -\chi\frac{\partial u^0}{\partial x}(x,H) + \hat{v}^1(x), \tag{A25}$$

where $\hat{v}^1(x)$ does not need to be specified, but it appears since v^1 is defined in (A24) up to a function of x. We gather from the above result that it is sufficient to integrate the equation of equilibrium at the order ε^0 over $\mathcal{Y}$, specifically,

$$\int_{\mathcal{Y}}\left[\mathrm{div}_{\boldsymbol{\chi}}\boldsymbol{\tau}^1 + \frac{\partial\tau_x^0}{\partial x} + \rho(\boldsymbol{\chi})\omega^2 u^0(x,H)\right]d\boldsymbol{\chi} = 0. \tag{A26}$$

It is now sufficient to use that $\tau_x^0 = 0$, and that $\boldsymbol{\tau}^1\cdot\boldsymbol{n} = 0$ on the interfaces with the air and is continuous in $\mathcal{Y}$, to get that

$$\lim_{\zeta\to-\infty}\left[-\int_{\mathsf{Y}_\mathrm{t}}\tau_z^1(x,\boldsymbol{\chi})d\chi + \omega^2 u^0(x,H)\int_{\mathcal{Y}}\rho(\boldsymbol{\chi})d\boldsymbol{\chi}\right] = 0. \tag{A27}$$

Integrating over Y_t the matching condition on $\boldsymbol{\tau}^1$ in (A20), we first get that

$$\lim_{\zeta\to-\infty}\left[\langle\sigma_z^1\rangle(x,H) + \zeta\frac{\partial\langle\sigma_z^0\rangle}{\partial z}(x,H) - \omega^2 u^0(x,H)\int_{\mathcal{Y}}\rho(\boldsymbol{\chi})d\boldsymbol{\chi}\right] = 0. \tag{A28}$$

In the above expression, there is a diverging term, linear in ζ, but this term cancels when using that $\int_{\mathcal{Y}}\rho(\boldsymbol{\chi})d\boldsymbol{\chi} = \int_{\mathcal{Y}_\mathrm{f}}\rho(\boldsymbol{\chi})d\boldsymbol{\chi} - (\zeta + H_\mathrm{f}/\ell)\rho_\mathrm{t}\varphi_\mathrm{t}$, along with (A10). It follows that

$$\langle\sigma_z^1\rangle(x,H) = -\left[\int_{\mathcal{Y}_\mathrm{f}}\frac{\rho(\boldsymbol{\chi})}{\rho_\mathrm{t}\varphi_\mathrm{t}}d\boldsymbol{\chi} - \frac{H_\mathrm{f}}{\ell}\right]\frac{\partial\sigma_z^0}{\partial z}(x,H). \tag{A29}$$

The expression that we use in our study corresponds to a homogeneous mass density of the foliage $\rho(\boldsymbol{\chi}) = \rho_\mathrm{f}$ and a filling fraction φ_f of foliage in $\mathcal{Y}_\mathrm{f}$, whence $\int_{\mathcal{Y}_\mathrm{f}}\rho(\boldsymbol{\chi})d\boldsymbol{\chi} = \rho_\mathrm{f}\varphi_\mathrm{f}H_\mathrm{f}/\ell$, resulting in

$$\langle\sigma_z^1\rangle(x,H) = -\frac{H_\mathrm{f}}{\ell}\left(\frac{\varphi_\mathrm{f}}{\varphi_\mathrm{t}}\frac{\rho_\mathrm{f}}{\rho_\mathrm{t}} - 1\right)\frac{\partial\sigma_z^0}{\partial z}(x,H). \tag{A30}$$

3. Effective jump condition at $z = 0$

These jump conditions have already been treated in [27] in the case where the two media, in the layer and in the trees, are identical; the derivation is similar in the present case and it is left to the reader. It is worth noting that more involved jump conditions can be found at the second order in ε, notably if heterogeneities as roots are considered at the tree bottom.

4. Definition of the unique problem

To get a unique problem, we consider the fields $(u^0 + \varepsilon\langle u^1\rangle)$ and $(\langle\boldsymbol{\sigma}^0\rangle + \varepsilon\langle\boldsymbol{\sigma}^1\rangle)$. It is sufficient to gather (i) (A10), (A13), and (A15) for $z \in (0,H)$, and (ii) (A22) and (A30) at the top of the trees. Doing so, we can write the problem $(\mathcal{S})$ satisfied by $(\langle u^0\rangle + \varepsilon\langle u^1\rangle)$ and $(\langle\boldsymbol{\sigma}^0\rangle + \varepsilon\langle\boldsymbol{\sigma}^1\rangle)$, and it is easy to see that u^e and $\boldsymbol{\sigma}^e$ satisfying (A2) admit the same

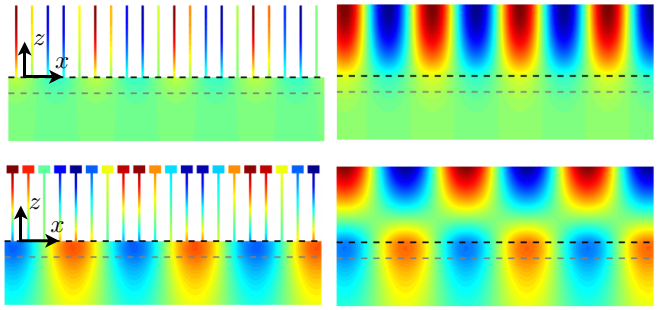

(a) $H = H_1$

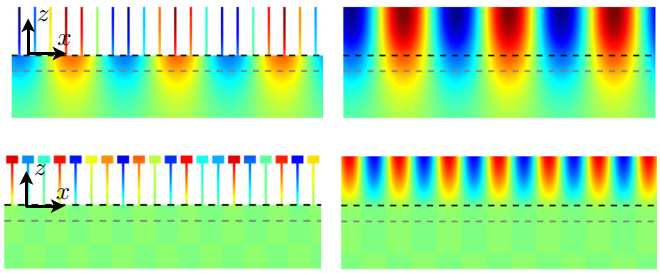

(b) $H = H_2$

FIG. 14. Displacement fields of the first spoof Love waves without and with foliage at $f = 30$ Hz and (a) $H = H_1 = 9$ m and (b) $H = H_2 = 6.2$ m (see black arrows in Fig. 5). The left panels show the actual displacement fields and the right panels show the corresponding homogenized fields, (5), (7) and (10), (11).

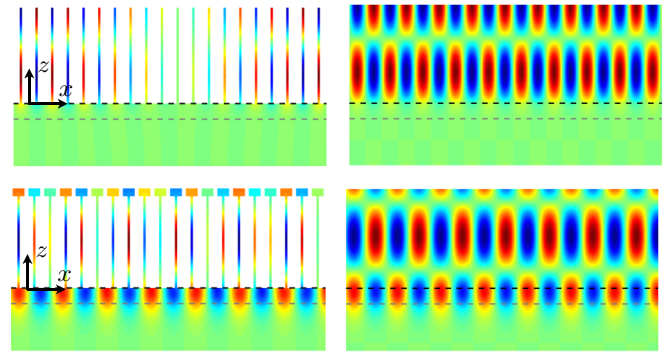

(a) $H = H_1$

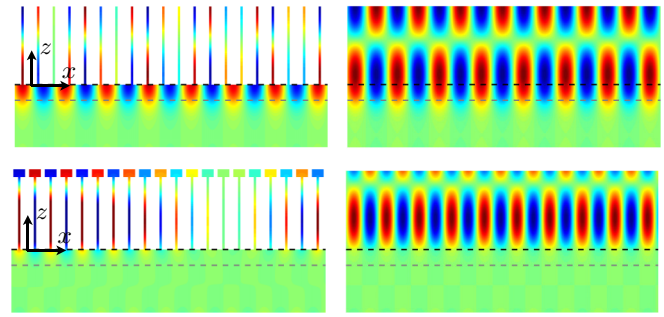

(b) $H = H_2$

FIG. 15. Displacement fields of the spoof Love waves for trees without and with foliage at $f = 70$ Hz; same representation as in Fig. 14.

asymptotic expansions as $(\langle u^0\rangle + \varepsilon\langle u^1\rangle)$ and $(\langle \boldsymbol{\sigma}^0\rangle + \varepsilon\langle \boldsymbol{\sigma}^1\rangle)$ up to $O(\varepsilon^2)$; thus the same expansion as u and $\boldsymbol{\sigma}$ in the real problem up to $O(\varepsilon^2)$.

APPENDIX B: WAVE FIELDS IN THE ACTUAL/HOMOGENIZED PROBLEMS

1. Trees of constant height

Here, we reported in Fig. 14(a) the displacement fields of the spoof Love waves at the upper limit of the band gap ($\beta = 1.5$ m^{-1}, close to π/ℓ) for a forest of trees of height $H_1 = 9$ m without foliage [black arrow in Fig. 5(a)]. For this high confinement, the guided wave is supported by the trees with almost zero amplitude in the guiding layer. When the trees support a foliage, the guided wave significantly changes its shape, being now close to a classical Love wave with $\beta \simeq 1$ m^{-1}. The reverse occurs for $H = H_2 = 6.2$ m corresponding to a highly confined guided wave in the presence of foliage and a classical Love wave in its absence; see Fig. 14(b). In the four considered cases, we report for comparison the homogenized fields given by (5) along with (7) [and (10) with (11)], which confirms the capacity of the model to predict the main features of the spoof Love wave. The same representation is used at $f = 70$ Hz in Fig. 15.

2. Trees of varying height: The wedge problem

The homogenized problem (3) has been implemented in the COMSOL MULTIPHYSICS finite-element package, treating the Robin condition in a way similar to what is described in Sec. 5.3 of [32]. Typical results at $f = 30$ and 70 Hz are reported in Fig. 16; the good agreement of Fig. 16(a) with Fig. 9(a), and Fig. 16(b) with Fig. 10(a), is noted.

APPENDIX C: EFFECTIVE IMPEDANCES IN A MASS-SPRING RESONATOR MODEL

Mass-spring models often make possible an easy and nice interpretation of the behaviors of resonant systems. The case of waves guided at the interface of an elastic solid supporting an array of mass springs has been considered in [22–25]. In general, the idea is to describe real mass-spring systems except in [23], where the mass spring is an idealization of an aluminium sheet with resonant bending oscillations. With M the mass and K the spring constant, the motion Y of a single resonator is described by

$$M\ddot{Y}_n = K(U_n - Y_n), \quad n = 1, 2, \ldots, \tag{C1}$$

where U_n is the surface displacement at the point of contact of the nth spring with the surface. In the harmonic regime, this yields a relation $Y_n = f(U_n, \omega)$. The next step consists of considering, in the limit of large wavelength compared to the array spacing, a continuous version of the discrete problem with

(i) $U_n = u(x, 0)$, which means that the displacement is merely constant in the unit cell; and

(ii) $F_n = \sigma_z(x, 0)\ell$, with $F_n = K(U_n - Y_n)$ the force exerted by the nth spring which is replaced by the mean surface

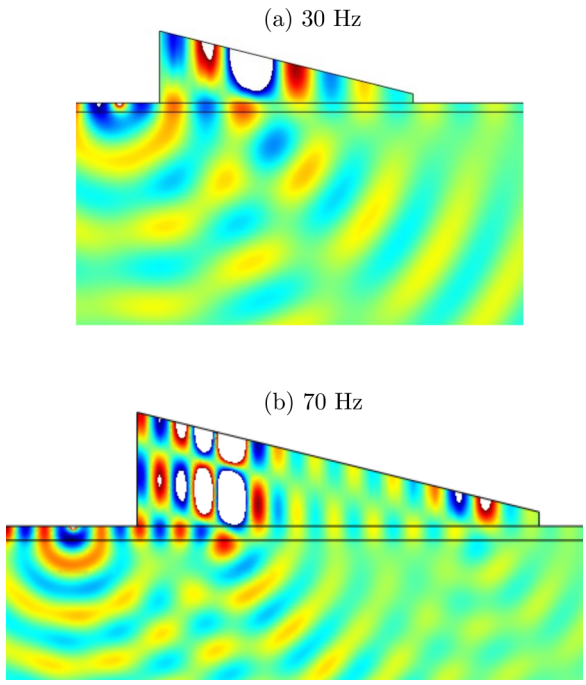

FIG. 16. Displacement fields of the spoof Love waves for an effective wedge described by homogenized equation (3) and boundary condition (4) on its upper boundary. The traction-free condition is applied on vertical sides, while the usual continuity of displacement and stress is applied at the interface between wedge and soil. Plots should be compared with those in Fig. 9(a) and Fig. 10(a).

stress (here on each period ℓ). Doing so, an effective boundary condition of the Robin's type can be derived, which takes the form

$$\sigma_z(x,0) = Z(\omega)\,u(x,0), \tag{C2}$$

and which reduces to the stress-free condition $\sigma_z = 0$ in the absence of springs. Inserting this condition in (5) along with the continuity of u and σ_z which still applies at $z = -e$ (and removing the solution written for $0 < z < H$) leaves us with a dispersion relation of the form

$$\left(\frac{\mu_\ell k_\ell}{\mu_s \alpha_s} + \frac{Z(\omega)}{\mu_\ell k_\ell}\right)\tan k_\ell e = 1 - \frac{Z(\omega)}{\mu_s \alpha_s}. \tag{C3}$$

In the case of actual mass springs such as considered in [25], the impedance $Z(\omega)$ is given by

$$Z(\omega) = \frac{M}{\ell}\frac{\omega^2\omega_0^2}{\omega_0^2 - \omega^2}, \tag{C4}$$

with $\omega_0 = \sqrt{K/M}$ the resonance frequency.

From the form of the homogenized solution in the trees $0 < z < H$ in (5), it is easy to see that a generalized Robin equation can be written, with now

$$Z(\omega) = \mu_t k_t \varphi_t \tan k_t H, \tag{C5}$$

in the absence of foliage and, from (10),

$$Z(\omega) = \mu_t k_t \varphi_t \frac{\tan k_t H + k_t L_e}{1 - k_t L_e \tan k_t H}, \tag{C6}$$

in the presence of foliage. Obviously, using (C5) [(C6)] in (C3), we recover the dispersion relation given in (7) [(11)]. The effective boundary condition (C3) along with (C5) is known in acoustics for slot resonators and it is derived in this context using approximate modal methods [33]. Expectedly, (C5) tells us that the trees without foliage behave essentially as slots with a quarter-wavelength resonance as lower resonance; as such, (C4) is a good approximation of (C5) locally near $\omega_0 = \pi c_t/(2H)$. The impedance (C6) accounting for the effect of the foliage is less intuitive. In particular, although L_e in (4) is linked to the added mass of the foliage, it is difficult to reduce its effect to an effective mass in a mass-spring model.

More generally, boundary-layer effects provide a family of effective boundary conditions more involved than that of the Robin's type. In particular and as previously stressed, higher-order models which are required if roots or other heterogeneities at the tree bottom are considered make jump conditions to appear which involve higher derivatives of the displacement field. In this case, the analogy is no longer possible, or let us say it becomes too convoluted to be enlightening.

APPENDIX D: NUMERICAL IMPLEMENTATION OF THE 3D ACTUAL PROBLEM ON COMSOL MULTIPHYSICS

In order to be consistent with the soil and tree parameters of Sec. III, we consider an elasticity tensor $C_{ijkl} = \lambda\delta_{ij}\delta_{kl} + \mu(\delta_{ik}\delta_{jl} + \delta_{il}\delta_{jk})$, $i, j, k, l = 1, 2, 3$, with $\lambda_s = 7.8 \times 10^8$ Pa, $\mu_s = 3.2 \times 10^8$ Pa, and $\rho_s = 1.3 \times 10^3$ kg m^{-3} for the substrate, $\lambda_\ell = 7.8 \times 10^8$ Pa, $\mu_\ell = 3.2 \times 10^8$ Pa, and $\rho_\ell = 2.6 \times 10^3$ kg m^{-3} for the guiding layer, and $\lambda_t = 7.8 \times 10^8$ Pa, $\mu_t = 6.68 \times 10^8$ Pa, and $\rho_t = 4.5 \times 10^2$ kg m^{-3} for the trees. In addition, we need to add perfectly matched layers to avoid reflections on the computational domain boundary, and here we chose to implement those described in [34] (involving a complex-valued anisotropic elasticity tensor without the minor symmetries and a complex-valued isotropic density) in the COMSOL finite-element package. Obviously, the computational task is more demanding than in the 2D case; for instance, the mesh consists of 200 000 tetrahedra, and thus we require more computational resources and we opt for a cluster of eight computers with Quadricore processors running at 2.24 GHz with a total of 1024 Gb of random-access memory.

The cubical computational domain of side length 100 m is surrounded by perfectly matched layers (PMLs) involving a complex-valued anisotropic elasticity tensor without the minor symmetries and a complex-valued isotropic density. More precisely, let us apply the following geometric transform in the Navier equations (see also [34] for the analogous case of three-dimensional elastic plates):

$$(x', y', z') = \left[\int_0^x s_1(\xi)d\xi\,,\ \int_0^y s_2(\xi)d\xi,\ \int_0^z s_3(\xi)d\xi\right]. \tag{D1}$$

The (x', y', z') are the working complex coordinates and the stretches $s_1(\xi), s_2(\xi), s_3(\xi)$ are either equal to 1 or to $(\xi/L)\ (1 - i)G$, depending on the direction along which one would like to absorb the wave. The width of the PML region L is a geometrical parameter that is automatically extracted for each region, whereas the dimensionless PMLs scaling factor

G is tuned in order to achieve the needed PMLs efficiency. These so-called adaptative PMLs were first proposed for electromagnetic waves; see [35]. The transformation (D1) is used to map the real-valued coefficients C_{ijkl} of the isotropic homogeneous elasticity tensor onto the complex-valued coefficients C_{ijkl}^{pml} of the anisotropic nonfully symmetric elasticity tensor in the PML region and the real-valued isotropic mass density ρ onto the complex-valued isotropic mass density ρ^{pml} in the PML region. For a bounded three-dimensional isotropic homogeneous elastic medium with Lamé coefficients λ, μ, the elastic coefficients in the PML region read

$$C_{ijkl}^{\text{pml}} = C_{ijkl}\frac{s_1 s_2 s_3}{s_i s_k}, \quad i, j, k, l = 1, 2, 3, \tag{D2}$$

and the density is as follows:

$$\rho^{\text{pml}} = s_1(x)s_2(y)s_3(z)\rho,$$

where further details on the efficiency of the adaptative elastic PMLs can be found in the 2D case in [34].

[1] L. Kelders, J. F. Allard, and W. Lauriks, J. Acoust. Soc. Am. **103**, 2730 (1998).
[2] J. B. Pendry, L. Martin-Moreno, and F. Garcia-Vidal, Science **305**, 847 (2004).
[3] P. Lalanne and J.-P. Hugonin, Nat. Phys. **2**, 551 (2006).
[4] N. Yu and F. Capasso, Nat. Mater. **13**, 139 (2014).
[5] K. L. Tsakmakidis, A. D. Boardman, and O. Hess, Nature (London) **450**, 397 (2007).
[6] M. S. Jang and H. Atwater, Phys. Rev. Lett. **107**, 207401 (2011).
[7] J. Zhu, Y. Chen, X. Zhu, F. J. Garcia-Vidal, X. Yin, W. Zhang, and X. Zhang, Sci. Rep. **3**, 1728 (2013).
[8] Y. Achaoui, A. Khelif, S. Benchabane, L. Robert, and V. Laude, Phys. Rev. B **83**, 104201 (2011).
[9] S. Brûlé, E. H. Javelaud, S. Enoch, and S. Guenneau, Phys. Rev. Lett. **112**, 133901 (2014).
[10] B. Gralak, S. Enoch, and G. Tayeb, J. Opt. Soc. Am. A **17**, 1012 (2000).
[11] S. Brûlé, E. H. Javelaud, S. Enoch, and S. Guenneau, Sci. Rep. **7**, 18066 (2017).
[12] A. Colombi, P. Roux, S. Guenneau, P. Gueguen, and R. V. Craster, Sci. Rep. **6**, 19238 (2016).
[13] A. Colombi, D. J. Colquitt, P. Roux, S. Guenneau, and R. V. Craster, Sci. Rep. **6**, 27717 (2016).
[14] D. J. Colquitt, A. Colombi, R. V. Craster, P. Roux, and S. Guenneau, J. Mech. Phys. Sol. **99**, 379 (2017).
[15] A. Colombi, V. Ageeva, J. R. Smith, A. Clare, R. Patel, M. Clark, D. J. Colquitt, P. Roux, S. Guenneau, and R. V. Craster, Sci. Rep. **7**, 6750 (2017).
[16] P. Roux, D. Bindi, T. Boxberger, A. Colombi, F. Cotton, I. Douste-Bacque, S. Garambois, P. Gueguen, G. Hillers, D. Hollis, T. Lecocq, and I. Pondaven, Seismological Res. Lett. **89**, 582 (2018).
[17] A. Palermo, S. Krodel, A. Marzani, and C. Daraio, Sci. Rep. **6**, 39356 (2016).
[18] A. E. H. Love, *Some Problems of Geodynamics* (Cambridge University Press, Cambridge, 1911).
[19] R. D. Woods, *Screening of Surface Waves in Soils*, Technical Report No. IP-804 (University of Michigan, Ann Arbor, MI, 1968).
[20] J.-F. Semblat and A. Pecker, *Waves and Vibrations in Soils: Earthquakes, Traffic, Shocks, Construction Works* (IUSS Press, Pavia, 2009).
[21] S. Brûlé and F. Cuira, AFNOR (2018).
[22] A. A. Maznev and V. E. Gusev, Phys. Rev. B **92**, 115422 (2015).
[23] C. Boutin, L. Schwan, and M. S. Dietz, J. Appl. Phys. **117**, 064902 (2015).
[24] A. Palermo, S. Krödel, K. H. Matlack, R. Zaccherini, V. K. Dertimanis, E. N. Chatzi, A. Marzani, and C. Daraio, Phys. Rev. Appl. **9**, 054026 (2018).
[25] A. Palermo and A. Marzani, Sci. Rep. **8**, 7234 (2018).
[26] J.-F. Mercier, M. L. Cordero, S. Félix, A. Ourir, and A. Maurel, P. Roy. Soc. London A **471**, 20150472 (2015).
[27] J.-J. Marigo and A. Maurel, SIAM J. Appl. Math. **77**, 721 (2017).
[28] A. Maurel, J.-J. Marigo, J.-F. Mercier, and K. Pham, Proc. R. Soc. A **474**, 20170894 (2018).
[29] A. Maurel, J.-J. Marigo, P. Cobelli, P. Petitjeans, and V. Pagneux, Phys. Rev. B. **96**, 134310 (2017).
[30] M. F. Yanik and S. Fan, Phys. Rev. Lett. **92**, 083901 (2004).
[31] M. Rupin, F. Lemoult, G. Lerosey, and P. Roux, Phys. Rev. Lett. **112**, 234301 (2014).
[32] K. Burla, A. V. Kumar, and B. V. Sankar, Int. Solids Struct. **46**, 2514 (2009).
[33] V. Romero-Garcìa, G. Theocharis, O. Richoux, and V. Pagneux, J. Acoust. Soc. Am. **139**, 3395 (2016).
[34] A. Diatta, Y. Achaoui, S. Brûlé, S. Enoch, and S. Guenneau, AIP Adv. **6**, 121707 (2016).
[35] G. Demésy, F. Zolla, A. Nicolet, M. Commandré, and C. Fossati, Opt. Exp. **15**, 18089 (2007).